metals

MDPI

Article

Evaluation of the Effect of Minor Additions in the Crystallization Path of $[(Fe_{0.5}Co_{0.5})_{0.75}B_{0.2}Si_{0.05}]_{100-x}M_x$ Metallic Glasses by Means of Mössbauer Spectroscopy

S. Leila Panahi [1], Parthiban Ramasamy [2,3], Francesc Masdeu [4], Mihai Stoica [5], Joan Torrens-Serra [6] and Pere Bruna [1,7,8,*]

1 Departament de Física, Universitat Politècnica de Catalunya, BarcelonaTech (UPC), Av. Eduard Maristany 16, 08019 Barcelona, Spain; seyedeh.leila.panahi@upc.edu
2 Erich Schmid Institute of Materials Science, Austrian Academy of Sciences, Jahnstraße 12, A-8700 Leoben, Austria; parthiban.ramasamy@oeaw.ac.at
3 Department of Mechanical Engineering, University of Dunaujvaros, Tancsics M. u. 1/A, H-2400 Dunaujvaros, Hungary
4 Departament d'Enginyeria Industrial i Construcció, Universitat de les Illes Balears, Cra. De de Valldemossa km 7.5, 07122 Palma de Mallorca, Spain; francesc.masdeu@uib.es
5 Laboratory of Metal Physics and Technology, Department of Materials, ETH Zurich, 8093 Zurich, Switzerland; mihai.stoica@mat.ethz.ch
6 Departament de Física, Universitat de les Illes Balears, Cra. de Valldemossa km 7.5, 07122 Palma de Mallorca, Spain; j.torrens@uib.es
7 Institut de Tècniques Energètiques (INTE), Av. Diagonal 647, 08028 Barcelona, Spain
8 Barcelona Research Center in Multiscale Science and Engineering, Av. Eduard Maristany 16, 08019 Barcelona, Spain
* Correspondence: pere.bruna@upc.edu; Tel.: +34-934-134-151

Abstract: Understanding the crystallization of metallic glasses is fundamental in the design of new alloys with enhanced properties and better glass-formability. The crystallization of a series of Fe-based metallic glasses of composition $[(Fe_{0.5}Co_{0.5})_{0.75}B_{0.2}Si_{0.05}]_{100-x}M_x$ (M = Mo, Nb and Zr) has been studied by means of differential scanning calorimetry and transmission Mössbauer spectroscopy. This latter technique allows the following of the microstructural evolution of the studied alloys through the identification and quantification of the several Fe-containing crystalline phases and also through the changes in the amorphous structure at the initial stages of crystallization. The results show that the crystallization products are the same for all the studied compositions (α-Fe, Fe_2B, $(FeCo)_{23}B_6$ and a paramagnetic remnant) although with different relative proportions and the crystallization of a phase without Fe in the alloys with Zr. Moreover, the addition of Zr favors the crystallization of α-Fe causing a detrimental effect on the glass forming ability, while the increase in Mo content up to 6 at% favors the crystallization of $(FeCo)_{23}B_6$. The different amount of α-Fe and borides is presented as a measure of the glass forming ability of this type of alloys.

Keywords: metallic glasses; Mössbauer spectroscopy; crystallization

check for updates

Citation: Panahi, S.L.; Ramasamy, P.; Masdeu, F.; Stoica, M.; Torrens-Serra, J.; Bruna, P. Evaluation of the Effect of Minor Additions in the Crystallization Path of $[(Fe_{0.5}Co_{0.5})_{0.75}B_{0.2}Si_{0.05}]_{100-x}M_x$ Metallic Glasses by Means of Mössbauer Spectroscopy. *Metals* **2021**, *11*, 1293. https://doi.org/10.3390/met11081293

Academic Editor: Qingping Cao

Received: 22 July 2021
Accepted: 13 August 2021
Published: 16 August 2021

1. Introduction

Nowadays, metallic glasses (MGs) are a well-established type of material, characterized by their lack of long-range order structure, that can be produced in several physical forms (powders [1], ribbons [2], coatings [3], microwires [4,5], bulks [6], magnetorheological fluids [7], etc.) and have a potential variety of applications in several fields: (a) magnetism, including sensors or choke coils [8,9]; (b) electrocatalysis, for example, in fuel cells [10]; (c) biomedicine with stents or orthopedic surgeries [11–14], (d) engineering, for example with the development of micro electro-mechanical (MEMs) devices [15] and in environmental applications like the catalytic degradation of toxic organic molecules [16] or radiation

shielding properties of newly developed FeBCSiP alloys [17]. In particular, Fe-based metallic glasses are especially interesting as they present unique characteristics in comparison with conventional Fe-based crystalline alloys [6,8]. However, metallic glasses present some drawbacks related to the production of bulk pieces and their brittleness [18]. In 2004, Shen and co-workers presented a new family of Fe-based glassy alloys, FeCoSiBNb, which could be cast in bulk form and have excellent functional properties and high strength [19,20]. Their thermal stability, microstructural evolution and crystallization kinetics, as well as functional properties, have been a matter of an extensive number of studies [21–26]. The large GFA in these alloys arises from the presence of a transition metal like Nb that stabilizes the supercooled liquid region and inhibits the crystallization [27]. Lots of efforts have been devoted to further enhance GFA. One of the main strategies to achieve this goal is by microalloying, i.e., adding small amounts of certain elements in order to increase the glass forming ability (GFA) of the alloy while maintaining and/or enhancing the functional or structural properties. Shen reported an enhancement of GFA by the addition of Zr only up to 1% [28]. Other transition metals like Mo and Y [29] also have a similar effect while Cr leave GFA unaffected but has a beneficial effect on the corrosion resistance and plasticity. Alloying of rare earths is a matter of discussion: Gd has been reported to deteriorate GFA [24,29] whereas Tb and Dy have a positive effect if not exceeding an optimal amount [30–32]. In these cases, to understand the effect of the minor additions on the stability of the amorphous structure and its crystallization route is fundamental for developing new alloys. Very recently, Ramasamy et al. [33] studied the effect of replacing Nb with Mo and Zr in a FeCoBSiNb bulk metallic glass. In their study, it was shown that the GFA of the alloys decreases with the substitution and even hinders the production of a bulk amorphous structure in the case of Zr. However, a certain amount of Mo instead of Nb increases the magnetic saturation and the plasticity. The use of Nb, Mo and Zr as alloying elements is for the potential enhancement of the glass forming ability caused by the introduction of a large radius mismatch and by the control of the size and type of phase during primary crystallization. Alloying elements produce changes in the local atomic configuration and short-range order of the glasses [34]. Moreover, it has recently shown by different authors that even nanoscale structural heterogeneities have a deep impact on their glass formability, crystallization and magnetic and mechanical properties [35–37]. Transmission Mössbauer Spectroscopy (TMS) is one of the few techniques, together with Extended X-Ray Absorption Fine Structure (EXAFS), able to obtain information on amorphous structures yielding insights on the local surroundings of the Fe atoms from variations in the hyperfine energy levels of the Fe nuclei. Moreover, the Mössbauer signal is directly proportional to the number of Fe atoms present in each phase, thus allowing the quantification of the relative amount of Fe atoms in a particular region, either crystalline or amorphous. This technique has been successfully used in combination with other conventional characterization techniques like x-ray diffraction or differential scanning calorimetry to offer a comprehensive view of the structure and phase formation not only in metallic glasses [26,29,38–40] but also in many Fe-containing alloys [41–43]. In the present paper, FeCoSiB(Nb,Zr,Mo) metallic glasses have been produced in ribbon shape in order to study their amorphous structure and their crystallization by means of Transmission Mössbauer Spectroscopy (TMS) and shed some light on the effects of the different elements (Nb, Zr and Mo) on this Fe-based metallic glass.

2. Materials and Methods

Five different compositions have been produced by the melt-spinning technique taking FeCoBSi as a base alloy. Namely, $[(Fe_{0.5}Co_{0.5})_{0.75}B_{0.2}Si_{0.05}]_{100-x}M_x$ with M = Mo, Nb and Zr and x = 4 for all M and x = 4, 5 and 6 for M = Mo. From now on, these compositions will be labelled Nb4, Zr4, Mo4, Mo5 and Mo6. All the alloys have been made from raw elements with high purity (>99.99%) in an arc melter with a water-cooled copper plate in a Ti-gettered Ar atmosphere and remelted three times to assure compositional homogeneity. The produced alloy has been subsequently melted in an induction coil in a melt spinner

with Ar atmosphere and injected into a rotating copper wheel with a tangential velocity of 40 m/s to produce the amorphous ribbons. The thermal characterization of the as-quenched ribbons has been made by means of Differential Scanning Calorimetry (DSC) in a NETZSCH DSC 404 (NETZSCH-Gerätebau GmbH, Graz, Austria) with a heating rate of 20 K min^{-1} under N_2 atmosphere with flow rate of 50 mL min^{-1}. The as-quenched ribbons have been annealed at selected temperatures for 5 min to follow-up the crystallization process. Transmission Mössbauer Spectroscopy (TMS) spectra at room temperature and pressure have been obtained with a constant acceleration spectrometer with a 25 mCi source of ^{57}Co in a Rh matrix. The spectra were recorded in a multichannel analyzer with 800 channels using a velocity range of $\pm$ 12 mm s^{-1}. Experimental spectra were fitted with Brand's NORMOS software (accessed on 3 May 2021) [44] using different fitting strategies depending on the microstructural state of the samples that will be described in the following section. The isomer shift values are given relative to the isomer shift of a Mössbauer spectrum of α-Fe recorded at room temperature. XRD diffractograms have been obtained using a Bruker-AXS D8 x-ray diffractometer (Bruker, Billerica, MA, USA) with Cu-Kα (λ = 0.15406 nm).

3. Results

The DSC thermograms of the five as-quenched ribbons are shown in Figure 1. The existence of a glass transition, although not clear in the Zr4 alloy, together with the main exothermic peak below 900 K demonstrate the amorphous character of the as produced ribbons. The crystallization behavior is, as expected, the same as the one observed in the same compositions produced as bulk metallic glasses [33]. The crystallization starts with a single exothermic peak followed by different less exothermic crystallization events. In the Nb4 alloy, an extended exothermic event is found up to 1023 K followed by a third peak, a similar path to that observed in very close alloys [19]. Mo-containing alloys, demonstrate a devitrification route which changes with the Mo content. For the alloy with 4% of Mo, four clear exothermic events are distinguishable in the thermogram: the primary crystallization is followed by an extended second exothermic peak up to 975 K (similar to that found in Nb4) and two more exothermic peaks at higher temperatures. The increase in Mo content induces the vanishing of the second peak and produces the shift of the third peak to higher temperatures whereas the fourth has an inverse tendency and seems to overlap. It is worth noting that the transformation enthalpy for the first crystallization reduces with Mo content. The DSC thermogram for Zr4 alloy shows clear differences to that of Nb- and Mo-containing alloys. Firstly, the second extended crystallization event is not observed following the primary crystallization peak. Instead, a narrow exothermic peak is distinguished at 1003 K followed by two overlapped exothermic peaks at higher temperatures.

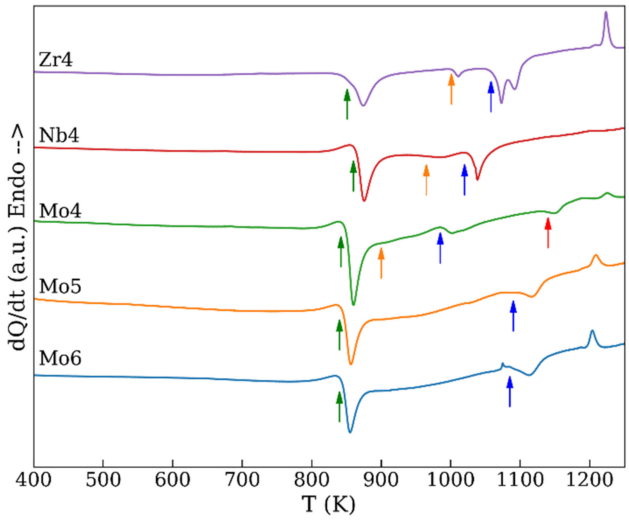

Figure 1. DSC curves of all five compositions at a heating rate of 20 K min^{-1}. The colored arrows indicate the onset temperature of the different crystallization events.

According to the thermal behavior observed in the DSC curves, each alloy has been annealed at different temperatures just after the crystallization peaks: main crystallization peak (T_1), just after the extended second peak (T_2) in Nb4, Mo4 and Mo5, and after the final crystallization event (T_F). Mo4 and Mo5 have been also annealed after the third crystallization peak (T_3). The corresponding values are shown in Table 1. The as-quenched ribbons, as well as the annealed ones at each temperature for each composition, have been analyzed by means of TMS. The different ribbons will be labelled as Mx-Ty where M = Zr, Nb, Mo, x = 4, 5, 6 and y = 1, 2, 3, F indicating the composition and the annealing temperature, respectively. The Mössbauer spectra of the as-quenched ribbons, as well as the ribbons annealed at T_1, are shown in Figure 2. The spectra of the as-quenched ribbons have been fitted with a single distribution of hyperfine magnetic fields between 0 and 39 T. The shape of these hyperfine magnetic fields, shown in Figure 3, is typical of amorphous ferromagnetic metallic glasses, thus revealing the amorphous character of the as-produced compositions.

Table 1. Annealing temperatures (in K) for each alloy.

Temperature	Zr4	Nb4	Mo4	Mo5	Mo6
T_1	900	910	891	885	875
T_2	1003	1023	975	1010	990
T_3	-	-	1056	1063	-
T_F	1093	1118	1169	1159	1169

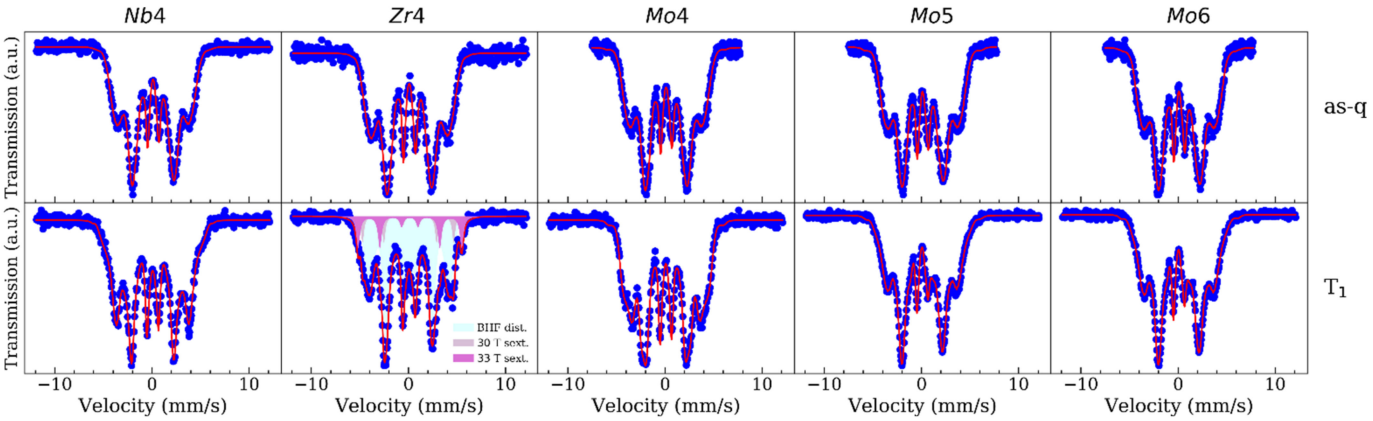

Figure 2. Experimental Mössbauer spectra (blue dots) and their fits (red line) for the as-quenched ribbons (top row) and the annealed ones at T_1 (bottom row). For Zr4-T1, the subspectra fitted for the different phases are also shown as filled areas.

There are no significant changes with composition in the hyperfine magnetic field distributions of the as-quenched ribbons, showing all of them a main broad peak between 20 and 25 T and a secondary peak between 10 and 15 T. The main difference between compositions is the average magnetic field of the distributions, shown in the inset of Figure 3, that is maximum for Zr4, decreases for Nb4 and further decreases with the increase in the Mo content of the alloy.

After the annealing at T_1, the shape of the spectra is similar to the as-quenched ones although the beginning of the crystallization can be observed in the shoulders of the spectra at around ± 6 mm/s. All the spectra have been fitted with a single hyperfine magnetic field distribution except Zr4-T1 in which two individual ferromagnetic sextets, with hyperfine magnetic fields of 33 and 30 T, have been needed to obtain a good fit in addition to the hyperfine field distribution, now between 0 and 32 T. The two sextets can be assigned to an α-Fe phase and to Fe atoms in an α-Fe phase with a non-magnetic element as near-neighbor, probably at the interface between the crystal and the amorphous matrix. The presence of α-Fe as the primary crystallization product is in accordance with the XRD diffractograms of this alloy published by Ramasamy [33].

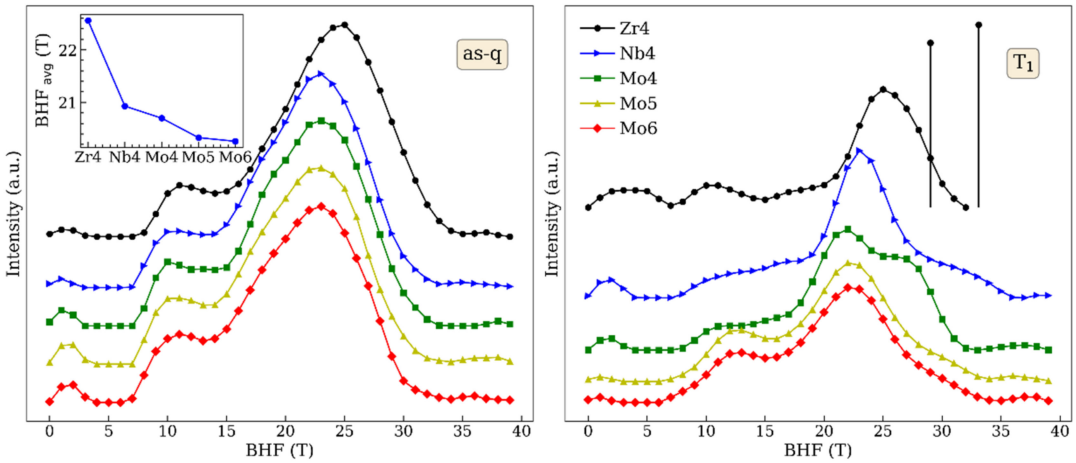

Figure 3. Experimental hyperfine magnetic field distributions for the as-quenched alloys (left) and the annealed ones at T_1 (right). The inset in the left panel shows the changes in the average hyperfine magnetic field as the composition changes. The two straight lines in the right panel correspond to the individual sextets at 30 and 33 T.

However, the changes in the short-range order of the annealed alloys can be clearly seen in the changes of the hyperfine field distribution. The annealing of the Nb4 alloy induces the reduction in the width of the main peak of the hyperfine field distribution (around 23 T) that also increases in intensity and the apparition of significant regions with hyperfine fields close to 33 T. This hyperfine field distribution has been associated with the formation of a $Fe_{23}B_6$-type phase in similar alloys [29] and is consistent with the identification from Synchrotron XRD [45].

In the Mo4-T1 alloy, the main peak has been split into two components at ~20 and ~26 T while the low field peak is reduced. These variations are not seen in Mo5-T1 and Mo6-T1 alloys that, on the contrary, show an increase in the intensity in the region around 30 T. To further understand them, XRD diffractograms of Mox-T1 have been recorded (see Figure 4). All three show the presence of Bragg peaks that are clearly identified as $Fe_{23}B_6$ phase and broad peaks that can be associated to an FeB-type phase. This latter identification is consistent with the peak between 10 and 15 T in the hyperfine field distributions as Fe environs close to an FeB phase have values of the hyperfine magnetic field in this range [29].

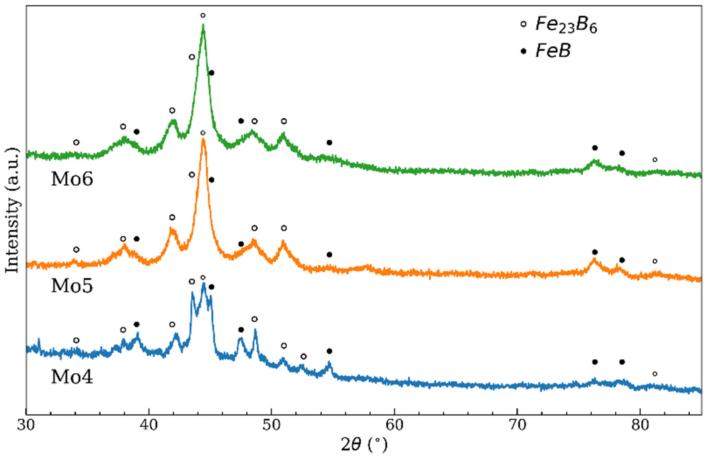

Figure 4. X-ray diffraction patterns of the Mo-containing samples annealed at T_1, just after the main crystallization peak.

However, in the Mo4-T1 sample, these peaks are narrower than in the other two alloys, which indicate that crystals have grown more in this alloy than in the other two. This hypothesis is consistent with the larger transformation enthalpy determined in the Mo4 first crystallization peak. These results are also in agreement with the result by Perea [46] that found that the presence of Mo promotes the precipitation of $Fe_{23}B_6$-type phase, as in Nb case. On the other hand, Zr4-T1 alloy, as already commented, is the one with the most significant changes with the presence of two individual sextets at high field values and also the formation of regions or environments in the alloy with low values of the hyperfine magnetic field (below 10 T). These low-magnetic areas, fitted for the sake of convenience with a hyperfine magnetic field distribution, in fact represent regions with a paramagnetic character. All these changes in the annealed alloys reflect the partial crystallization process of the alloys resulting in a microstructure composed of an amorphous ferromagnetic matrix with embedded crystalline particles.

The annealing at T_2 drastically changes the Mössbauer spectra of the studied alloys as the crystallization process progresses and, thus, the crystalline fraction increases. The spectra, shown in Figure 5, have been fitted with three sextets to take into account the ferromagnetic phases and one singlet for the paramagnetic phase. However, in the Mo-containing alloys, the paramagnetic singlet has been substituted by a hyperfine field distribution between 0 and 20 T that represents the remnants of the amorphous matrix and in Mo5 and Mo6 an extra sextet has been needed. The sextet with the highest value of the hyperfine field, around 33 T, corresponds to the crystallization of α-Fe and its area is maximum for the Zr4 alloy, followed by the Nb4, while the presence of Mo seems to present difficulties for the growing of this phase. The two other sextets, at around 24 T and 22 T, can be assigned to the crystallization of some iron borides. The former has values of the isomer shift between 0.04 and 0.1 mm s^{-1} and quadrupole splittings between 0 and −0.1 mm s^{-1} that fit well with the hyperfine parameters of a Fe_2B phase [29]. The latter presents isomer shift values around 0.09 mm s^{-1} and quadrupole splittings around −0.05 mm s^{-1}, closely matching the values for a $(FeCo)_{23}B_6$ phase [29]. The extra sextet for the Mo5 and Mo6 alloy, with a field of 20.6 T can be associated with a second iron environment in the $(FeCo)_{23}B_6$ phase [47]. The final annealing at T_F does not significantly change the Mössbauer spectra of the Nb4 and Zr4 alloys that present the same crystallization products as in the previous annealing with only slight differences in the relative intensities of each phase due to the crystalline growth with temperature and the transformation of the metastable boride phases. However, the Mo-containing samples show two main changes: (a) the important growth of the sextet corresponding to the α-Fe phase and (b) the transformation of the remaining amorphous matrix, that was fitted with a hyperfine magnetic field distribution in Mox-T2 alloys, into a paramagnetic single crystalline phase fitted with a singlet with an isomer shift close to zero. The intermediate annealing of Mo4 and Mo5 at T_3 does not introduce significant changes in the Mössbauer spectra besides slight changes in the relative amount of each phase that represent the growth or stabilization of the phases between T_3 and T_F.

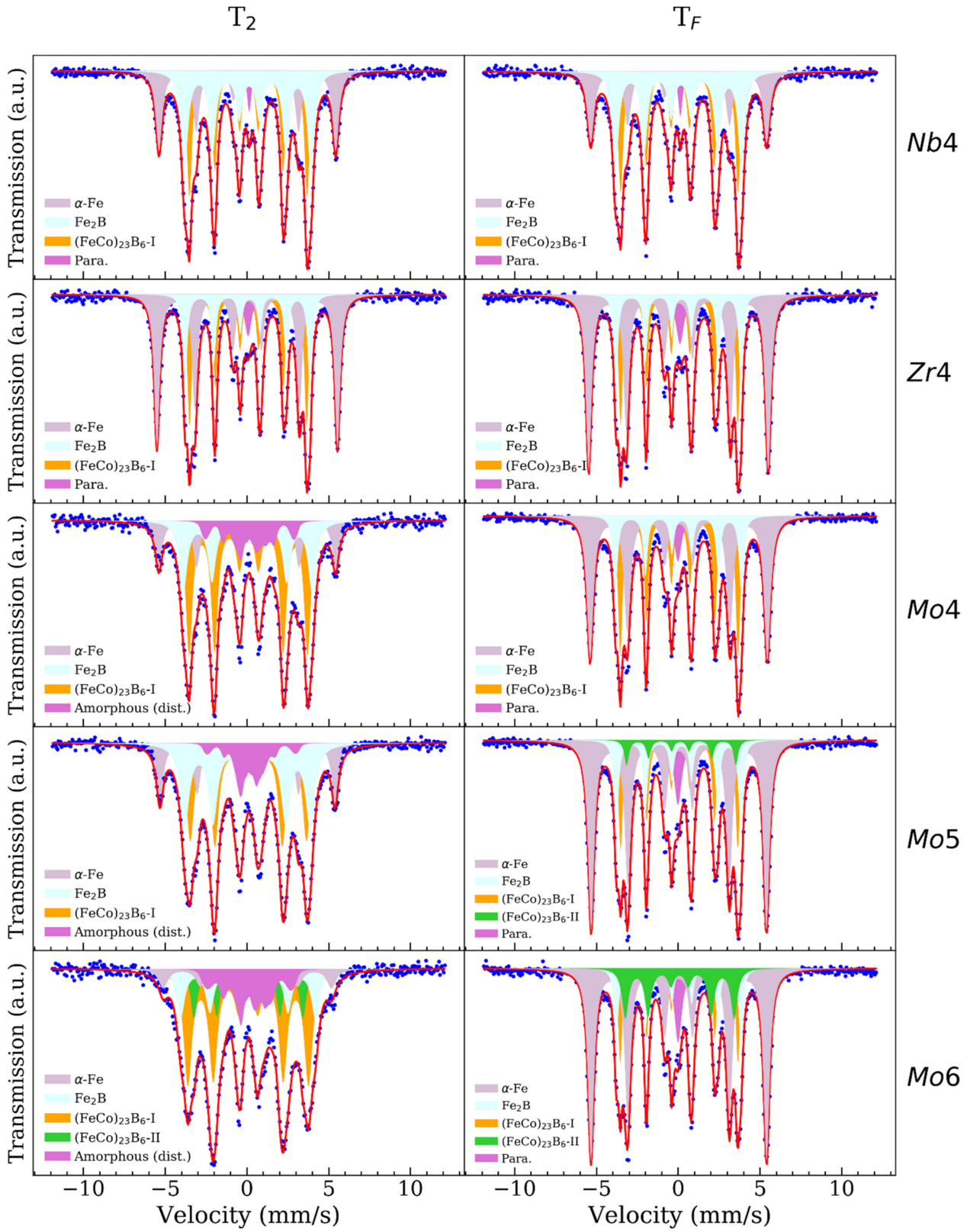

Figure 5. Experimental Mössbauer spectra (blue dots) and their fits (red line) for the ribbons annealed at T_2 (left column) and the annealed ones at T_3 (right column). The subspectra fitted for the different phases are also shown as filled areas.

4. Discussion

The previous results from Mössbauer spectroscopy clearly show that the crystallization products of all the samples are the same although the relative amount of each phase and its first apparition changes depending on the type and amount of the minor addition to the base composition. These phases are α-Fe, Fe_2B, $(FeCo)_{23}B_6$ and a paramagnetic phase. Therefore, the different DSC trace of the Zr4 alloy shown in Figure 1 may be attributed to the crystallization of an additional phase without Fe, thus invisible to the Mössbauer spectroscopy. According to [33], this phase could be identified as ZrB_2. One of the main advantages of Mössbauer spectroscopy is the ability to quantify the relative amount of Fe atoms in each phase at different stages of the crystallization process that is shown in Figure 6.

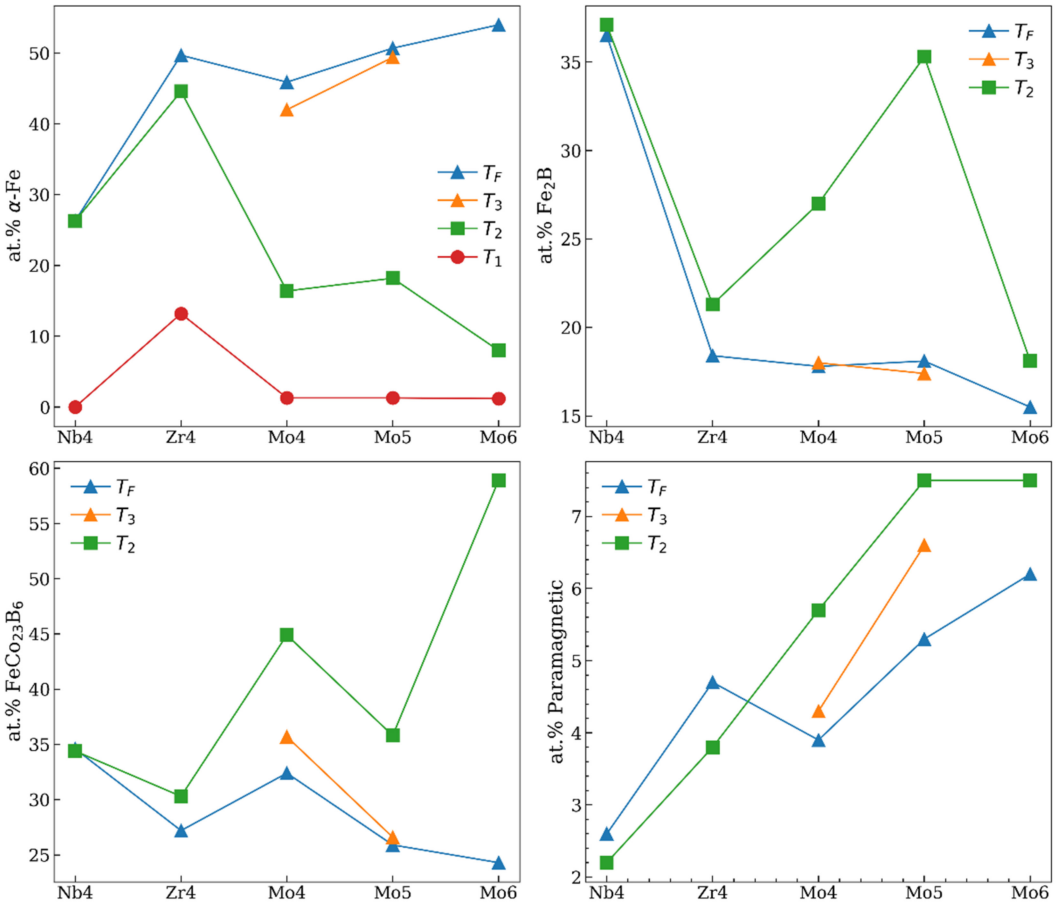

Figure 6. Percentage (relative to the total amount of Fe) of Fe atoms in the different crystalline phases as a function of the composition and the annealing temperature. The error bar in the at% is smaller than the symbols (the lines are guides to the eye).

Regarding the crystallization of α-Fe, it is clear that after the first annealing at T_1 only the Zr4 alloy shows the presence of this phase, as was already commented in the description of the Mössbauer spectra at T_1 in Figure 2. The subsequent annealings induce the growing of this phase that is almost complete after the annealing at T_2 in the Nb4 and Zr4 alloys while for the Mo-containing samples, the maximum growth of α-Fe is produced after the last annealing. The maximum amount of this phase, around 50 at%, is achieved for the Zr4 and Mo samples being almost the double of the α-Fe present in the fully crystalline Nb4 sample. The earlier formation of α-Fe in the Zr4 alloy can be explained by the fact that the hyperfine magnetic field distribution of this alloy is the one with a higher value of the average hyperfine field (see inset of Figure 3) and, thus with a higher amount of Fe atoms in environs with values of the hyperfine magnetic field around 30 T (see Figure 3) that will

easily transform to α-Fe. On the contrary, the evolution of the boride phases is the inverse, after an initial growth of these phases the last annealing reduces the presence of borides in the fully crystalline samples of all the compositions except in Nb4. In this alloy, the amount of Fe_2B and $(FeCo)_{23}B_6$ remains constant after annealing at T_2 and, in fact, the total amount of α-Fe, Fe_2B and $(FeCo)_{23}B_6$ is similar. Therefore, the addition of Nb to the base alloy induces the stabilization of boride's phases. The addition of Zr or Mo hinders the growth of Fe_2B in the fully crystalline samples while there are no significant changes in the amount of $(FeCo)_{23}B_6$. However, there are clear changes in the amount of both borides after the annealing at T_2 in the different Mo-containing alloys. At these intermediate temperatures the addition of Mo, from 4 to 5 at%, favors the formation of Fe_2B instead of $(FeCo)_{23}B_6$ while the addition of 6 at% changes drastically the situation and the $(FeCo)_{23}B_6$ phase reaches its maximum close to the 60 at%. It is worth to comment that in the Mo5 and Mo6 alloys it has been possible to assign two sextets corresponding to two different local environs around the Fe nucleus in the $(FeCo)_{23}B_6$ phase. This has been possible in part due to the high amount of this phase but especially due to the relative simplicity of the Mössbauer spectra with few crystalline phases and almost no amorphous remnants that usually make the interpretation of the spectra more difficult [29]. This result could be helpful in further studies of similar compositions in order to disentangle several simultaneous contributions to the spectra. In these situations, the number of possible interpretations yielding the same final fitting make impossible to obtain detailed information on the microstructure, unless one can support the assumptions on previous results as the one found here. Finally, we need to use a paramagnetic phase to obtain a good fit to the Mössbauer spectra. This paramagnetic phase is more present in the Mo-containing alloys after the annealing at T_2 although in the fully crystalline samples, in all the compositions, a similar amount is found and close to the 5 at%. It is also worth to mention that in the fully crystalline samples, where in all the compositions the paramagnetic phase has been fitted with a singlet, the corresponding isomer shift for the Mo samples is close to 0 mm s^{-1} while for the Nb and Zr samples is close to 0.1 mm s^{-1}, thus revealing different Fe environs. In order to obtain more information on these environs, two different studies can be performed. On the one side, a reduction in the velocity range of the Mössbauer spectra will increase the resolution on the central part of the spectra giving the possibility to shed some light on the chemical state of the Fe atoms in these environs. On the other side, the use of synchrotron radiation could yield diffraction spectra with high resolution and could be possible to detect and identify the crystalline structures that gives rise to the paramagnetic part of the Mössbauer spectra.

These results can be related with the glass forming ability (GFA) found for the bulk versions of these same compositions [33]. Ramasamay et al. found the best GFA for the Nb4 sample (bulk sample with a critical diameter of 3 mm). The Mössbauer results shown in the present paper can explain the best GFA for Nb4 alloy in terms of a competition of phases. On the one hand, the presence of Zr favors the crystallization of α-Fe, thus confirming that Mo and Nb samples should have a better GFA. Shen showed that the addition of Zr reduces the GFA if content is over 1% [28]. On the other hand, taking into consideration only Nb and Mo samples we can compute the relative amount of α-Fe with respect the total amount of iron atoms in environs close to an iron boride structure after the first annealing temperature (shown in Table 2). This ratio is higher for the Nb4 alloy and decreases with the addition of Mo, with the same behavior of the critical diameter, that is maximum for Nb4 and decreases with the Mo content. A ratio equal to 1 would mean that the amorphous structure is prone to crystallize into α-Fe and into iron borides with the same probability, thus creating two alternatives in the crystallization path and resulting in a more stable amorphous structure. Therefore, for the Nb4 alloy, where this ratio is higher, the competition between the crystallization of α-Fe and iron borides is higher than in the Mo alloys and resulting in its higher GFA. It is clear that correlation is not causation and, thus, the usefulness of this ratio should be checked studying other compositions (new or already published). The effect of partial substitution of Nb by Mo has been studied in other Fe-based metallic glasses. Zhu et al. [48] concluded that partial replacement of Nb

by Mo increases GFA in Fe(Nb,Mo)B alloys. This experimental result is also observed in FeBSi(Nb,Mo) alloys by Li [49].

Table 2. Ratio of α-Fe/Fe-borides and critical diameter, d_c, (from [33]) for Nb and Mo-containing samples.

	Nb4	Mo4	Mo5	Mo6
α-Fe/Fe-borides	0.37	0.23	0.26	0.1
d_c (mm)	3	1.5	1.5	1

5. Conclusions

In this paper a series of FeCoBSi metallic glasses with different additions of Nb, Zr and Mo have been studied by means of transmission Mössbauer Spectroscopy. The crystallization path of the different compositions and the changes in the local structure due to the different annealings have been followed through the changes in the hyperfine magnetic field distributions and the relative quantification of the iron containing phases. It has been shown how the presence of Zr induces the growth of α-Fe and changes the crystallization path with respect Nb- and Mo-containing alloys. Instead, the presence of small amounts of Mo favors the crystallization of Fe_2B while an addition of 6 at% of Mo yields the maximum amount of $(FeCo)_{23}B_6$ phase after the second annealing temperature. This high amount of this phase has allowed its fitting using two different sextets for two different environs of the Fe nucleus, result that can be useful for the interpretation of more complex spectra of similar compositions. Finally, the higher glass forming ability of the Nb-containing alloys has been explained by means of a competition between the crystallization of α-Fe, on the one side, and of iron borides, on the other side and a possible way to quantify this competition has been introduced in terms of the ratio between the at% of Fe nucleus present in each type of phase.

Author Contributions: Conceptualization, P.B. and J.T.-S.; methodology, P.B. and J.T.-S.; investigation, S.L.P., P.R., F.M., J.T.-S. and P.B.; resources, P.B.; writing—original draft preparation, P.B.; writing—review and editing, P.B., M.S. and J.T.-S.; supervision, P.B. All authors have read and agreed to the published version of the manuscript.

Funding: This research was funded by Generalitat de Catalunya through a FI grant 2018FI_B_00502, by MINECO grants (AEI/FEDER,UE) FIS2017-82625-P and RTI2018-094683-B-C51, and from Generalitat de Catalunya grant 2017-SGR-42. P.R. gratefully acknowledge additional support through the Shenzhen International Cooperation Research GJHZ20190822095418365.

Institutional Review Board Statement: Not applicable.

Informed Consent Statement: Not applicable.

Data Availability Statement: The raw/processed data required to reproduce these findings can be shared upon request to the corresponding author.

Conflicts of Interest: The authors declare no conflict of interest. The funders had no role in the design of the study; in the collection, analyses, or interpretation of data; in the writing of the manuscript, or in the decision to publish the results.

References

1. Zarazúa-Villalobos, L.; Mary, N.; Soo-Hyun, J.; Ogawa, K.; Kato, H.; Ichikawa, Y. Microstructure and corrosion study of Fe-based bulk metallic glass obtained by spark plasma sintering. *J. Alloys Compd.* **2021**, *880*, 160399. [CrossRef]
2. Yüce, E.; Sarac, B.; Ketov, S.; Reissner, M.; Eckert, J. Effects of Ni and Co alloying on thermal, magnetic and structural properties of Fe-(Ni,Co)-P-C metallic glass ribbons. *J. Alloys Compd.* **2021**, *872*, 159620. [CrossRef]
3. Liu, L.; Zhang, C. Fe-based amorphous coatings: Structures and properties. *Thin Solid Films* **2014**, *561*, 70–86. [CrossRef]
4. Liao, W.B.; Jiang, C.; Xu, S.; Gao, L.; Zhang, H.; Li, P.; Liu, Z.; Lu, Y. Reliability of tensile fracture strength of Co-based metallic glass microwires by Weibull statistics. *Mater. Res. Express* **2019**, *6*, 106565. [CrossRef]
5. Yin, H.; Law, J.; Huang, Y.; Franco, V.; Shen, H.; Jiang, S.; Bao, Y.; Sun, J. Design of Fe-containing GdTbCoAl high-entropy-metallic-glass composite microwires with tunable Curie temperatures and enhanced cooling efficiency. *Mater. Des.* **2021**, *206*, 109824. [CrossRef]

6. Li, H.X.; Lu, Z.C.; Wang, S.L.; Wu, Y.; Lu, Z.P. Fe-based bulk metallic glasses: Glass formation, fabrication, properties and applications. *Prog. Mater. Sci.* **2019**, *103*, 235–318. [CrossRef]
7. Yu, M.; Yang, C.; Bian, X.; Zhao, S.; Wang, T.; Liu, S.; Guo, T. Application of Fe78Si9B13 amorphous particles in magnetorheological fluids. *RSC Adv.* **2016**, *6*, 22511–22518. [CrossRef]
8. Suryanarayana, C.; Inoue, A. Iron-based bulk metallic glasses. *Int. Mater. Rev.* **2013**, *58*, 131–166. [CrossRef]
9. Lee, H.; Lee, A.Y.; Kim, K.I.; Jeong, H.; Hong, S.A.; Kim, M.; Lee, K.; Kim, K.T. Nano-crystallization behavior and magnetic domain evolution in commercial Fe–Si–B metallic glass. *J. Alloys Compd.* **2021**, *857*, 157565. [CrossRef]
10. Hu, Y.C.; Sun, C.; Sun, C. Functional Applications of Metallic Glasses in Electrocatalysis. *ChemCatChem* **2019**, *11*, 2401–2414. [CrossRef]
11. Li, H.F.; Zheng, Y.F. Recent advances in bulk metallic glasses for biomedical applications. *Acta Biomater.* **2016**, *36*, 1–20. [CrossRef] [PubMed]
12. Qin, C.; Hu, Q.; Li, Y.; Wang, Z.; Zhao, W.; Louzguine-Luzgin, D.V.; Inoue, A. Novel bioactive Fe-based metallic glasses with excellent apatite-forming ability. *Mater. Sci. Eng. C* **2016**, *69*, 513–521. [CrossRef] [PubMed]
13. Rajan, S.T.; Arockiarajan, A. Thin film metallic glasses for bioimplants and surgical tools: A review. *J. Alloys Compd.* **2021**, *876*, 159939. [CrossRef]
14. Wong, P.C.; Song, S.M.; Nien, Y.Y.; Wang, W.R.; Tsai, P.H.; Wu, J.L.; Jang, J.S.C. Mechanical properties enhanced by the dispersion of porous Mo particles in the biodegradable solid and bi-phase core–shell structure of Mg-based bulk metallic glass composites for applications in orthopedic implants. *J. Alloys Compd.* **2021**, *877*, 160233. [CrossRef]
15. Ashby, M.; Greer, A. Metallic glasses as structural materials. *Scr. Mater.* **2006**, *54*, 321–326. [CrossRef]
16. Zhang, L.; Qiu, L.; Zhu, Q.; Liang, X.; Huang, J.; Yang, M.; Zhang, Z.; Ma, J.; Shen, J. Insight into efficient degradation of 3,5-dichlorosalicylic acid by Fe-Si-B amorphous ribbon under neutral condition. *Appl. Catal. B Environ.* **2021**, *294*, 120258. [CrossRef]
17. Alshahrani, B.; Olarinoye, I.O.; Mutuwong, C.; Sriwunkum, C.; Yakout, H.A.; Tekin, H.O.; Al-Buriahi, M.S. Amorphous alloys with high Fe content for radiation shielding applications. *Radiat. Phys. Chem.* **2021**, *183*, 109386. [CrossRef]
18. Suryanarayana, C.; Inoue, A. *Bulk Metallic Glasses*, 2nd ed.; CRC Press: Boca Raton, FL, USA, 2017. [CrossRef]
19. Inoue, A.; Shen, B.L.; Chang, C.T. Super-high strength of over 4000 MPa for Fe-based bulk glassy alloys in [(Fe1-xCox)0.75B0.2Si 0.05]96Nb4 system. *Acta Mater.* **2004**, *52*, 4093–4099. [CrossRef]
20. Shen, B.; Inoue, A.; Chang, C. Superhigh strength and good soft-magnetic properties of (Fe,Co) -B-Si-Nb bulk glassy alloys with high glass-forming ability. *Appl. Phys. Lett.* **2004**, *85*, 4911–4913. [CrossRef]
21. Di, S.; Wang, Q.; Zhou, J.; Shen, Y.; Li, J.; Zhu, M.; Yin, K.; Zeng, Q.; Sun, L.; Shen, B. Enhancement of plasticity for FeCoBSiNb bulk metallic glass with superhigh strength through cryogenic thermal cycling. *Scr. Mater.* **2020**, *187*, 13–18. [CrossRef]
22. Fornell, J.; González, S.; Rossinyol, E.; Suriñach, S.; Baró, M.D.; Louzguine-Luzgin, D.V.; Perepezko, J.H.; Sort, J.; Inoue, A. Enhanced mechanical properties due to structural changes induced by devitrification in Fe-Co-B-Si-Nb bulk metallic glass. *Acta Mater.* **2010**, *58*, 6256–6266. [CrossRef]
23. Lesz, S.; Babilas, R.; Nabiałek, M.; Szota, M.; Dośpiał, M.; Nowosielski, R. The characterization of structure, thermal stability and magnetic properties of Fe-Co-B-Si-Nb bulk amorphous and nanocrystalline alloys. *J. Alloys Compd.* **2011**, *509* (Suppl. 1), S197–S201. [CrossRef]
24. Ramasamy, P.; Stoica, M.; Taghvaei, A.H.; Prashanth, K.G.; Kumar, R.; Eckert, J. Kinetic analysis of the non-isothermal crystallization process, magnetic and mechanical properties of FeCoBSiNb and FeCoBSiNbCu bulk metallic glasses. *J. Appl. Phys.* **2016**, *119*, 073908. [CrossRef]
25. Shen, B.; Chang, C.; Inoue, A. Formation, ductile deformation behavior and soft-magnetic properties of (Fe,Co,Ni)-B-Si-Nb bulk glassy alloys. *Intermetallics* **2007**, *15*, 9–16. [CrossRef]
26. Torrens-Serra, J.; Bruna, P.; Stoica, M.; Roth, S.; Eckert, J. Glass forming ability, thermal stability, crystallization and magnetic properties of [(Fe,Co,Ni)0.75Si0.05B0.20] 95Nb4Zr1 metallic glasses. *J. Non-Cryst. Solids* **2013**, *367*, 30–36. [CrossRef]
27. Inoue, A.; Shen, B. Soft magnetic bulk glassy Fe-B-Si-Nb alloys with high saturation magnetization above 1.5 T. *Mater. Trans.* **2002**, *43*, 766–769. [CrossRef]
28. Shen, B.; Chang, C.; Zhang, Z.; Inoue, A. Enhancement of glass-forming ability of FeCoNiBSiNb bulk glassy alloys with superhigh strength and good soft-magnetic properties. *J. Appl. Phys.* **2007**, *102*, 023515. [CrossRef]
29. Torrens-Serra, J.; Bruna, P.; Stoica, M.; Eckert, J. Glass-forming ability and microstructural evolution of [(Fe0.6Co0.4)0.75Si0.05B0.20]96-xNb4Mx metallic glasses studied by Mössbauer spectroscopy. *J. Alloys Compd.* **2017**, *704*, 748–759. [CrossRef]
30. Li, J.W.; He, A.N.; Shen, B.L. Effect of Tb addition on the thermal stability, glass-forming ability and magnetic properties of Fe-B-Si-Nb bulk metallic glass. *J. Alloys Compd.* **2014**, *586*, S46–S49. [CrossRef]
31. Li, J.; Men, H.; Shen, B. Soft-ferromagnetic bulk glassy alloys with large magnetostriction and high glass-forming ability. *AIP Adv.* **2011**, *1*, 042110. [CrossRef]
32. Li, J.; Yang, W.; Zhang, M.; Chen, G.; Shen, B. Thermal stability and crystallization behavior of (Fe 0.75—XDyxB0.2Si0.05) 96Nb4 (x = 0–0.07) bulk metallic glasses. *J. Non. Cryst. Solids* **2013**, *365*, 42–46. [CrossRef]
33. Ramasamy, P.; Stoica, M.; Bera, S.; Calin, M.; Eckert, J. Effect of replacing Nb with (Mo and Zr) on glass forming ability, magnetic and mechanical properties of FeCoBSiNb bulk metallic glass. *J. Alloys Compd.* **2017**, *707*, 78–81. [CrossRef]

34. Hirata, A.; Guan, P.; Fujita, T.; Hirotsu, Y.; Inoue, A.; Yavari, A.R.; Sakurai, T.; Chen, M. Direct observation of local atomic order in a metallic glass. *Nat. Mater.* **2011**, *10*, 28–33. [CrossRef] [PubMed]
35. Hirata, A. Local structure analysis of amorphous materials by angstrom-beam electron diffraction. *Microscopy* **2021**, *70*, 171–177. [CrossRef]
36. Idrissi, H.; Ghidelli, M.; Béché, A.; Turner, S.; Gravier, S.; Blandin, J.J.; Raskin, J.P.; Schryvers, D.; Pardoen, T. Atomic-scale viscoplasticity mechanisms revealed in high ductility metallic glass films. *Sci. Rep.* **2019**, *9*, 13426. [CrossRef]
37. Gemma, R.; to Baben, M.; Pundt, A.; Kapaklis, V.; Hjörvarsson, B. The impact of nanoscale compositional variation on the properties of amorphous alloys. *Sci. Rep.* **2020**, *10*, 11410. [CrossRef]
38. Babilas, R.; Spilka, M.; Młynarek, K.; Łoński, W.; Łukowiec, D.; Radoń, A.; Kądziołka-Gaweł, M.; Gębara, P. Glass-forming ability and corrosion resistance of Al88Y8-xFe4+x (x = 0, 1, 2 at.%) alloys. *Materials* **2021**, *14*, 1581. [CrossRef]
39. Kolano-Burian, A.; Zackiewicz, P.; Grabias, A.; Wojcik, A.; Maziarz, W.; Szlezynger, M.; Wlodarczyk, P.; Kowalczyk, M.; Hawelek, L. Effect of Co Substitution and Thermo-Magnetic Treatment on the Structure and Induced Magnetic Anisotropy of Fe84.5−xCoxNb5B8.5P2 Nanocrystalline Alloys. *Materials* **2021**, *14*, 3433. [CrossRef]
40. Ahmadian Baghbaderani, H.; Masood, A.; Alvarez, K.L.; Mathúna, C.; McCloskey, P.; Stamenov, P. CALPHAD-assisted development of in-situ nanocrystallised melt-spun Co-Fe-B alloy with high Bs (1.57 T). *J. Alloys Compd.* **2021**, *877*, 160194. [CrossRef]
41. Rivera, A.M.M.; López, J.E.R.; Munevar, J.; Saitovitch, E.B.; Aldana, L.C.M.; Vargas, C.A.P. Synthesis and characterization of the structural and magnetic properties of the Sm3-xGdxFe5O12(x = 0.0–1.0) garnets using solid-state reaction and citrate methods. *J. Alloys Compd.* **2021**, *859*, 157883. [CrossRef]
42. Popkov, V.I.; Martinson, K.D.; Kondrashkova, I.S.; Enikeeva, M.O.; Nevedomskiy, V.N.; Panchuk, V.V.; Semenov, V.G.; Volkov, M.P.; Pleshakov, I.V. SCS-assisted production of EuFeO3 core-shell nanoparticles: Formation process, structural features and magnetic behavior. *J. Alloys Compd.* **2021**, *859*, 157812. [CrossRef]
43. John, S.P.; Mathew, M.J. Determination of ferrimagnetic and superparamagnetic components of magnetization and the effect of particle size on structural, magnetic and hyperfine properties of Mg0.5Zn0.5Fe2O4 nanoparticles. *J. Alloys Compd.* **2021**, *869*, 159242. [CrossRef]
44. Brand, R. *NORMOS-90 Mössbauer Fitting Program Package*; Wissel GmbH: Starnberg, Germany, 1990.
45. Stoica, M.; Li, R.; Yavari, A.R.; Vaughan, G.; Eckert, J.; Van Steenberge, N.; Romera, D.R. Thermal stability and magnetic properties of FeCoBSiNb bulk metallic glasses. *J. Alloys Compd.* **2010**, *504*, S123–S128. [CrossRef]
46. Perea, D.; Parra, C.; Ramasamy, P.; Stoica, M.; Eckert, J.; Bolívar, F.; Echeverría, F. Structural and phase evolution upon annealing of Fe76 Si9−x B10 P5 Mox (X = 0, 1, 2 and 3) alloys. *Metals* **2020**, *10*, 881. [CrossRef]
47. Barinov, V.A.; Tsurin, V.A.; Surikov, V.T. DAPO effect in Fe23B6. *Phys. Met. Metallogr.* **2012**, *113*, 48–61. [CrossRef]
48. Zhu, M.; Zhang, M.; Yao, L.; Nan, R.; Jian, Z.; Chang, F. Effect of Mo substitution for Nb on the glass-forming ability, magnetic properties, and electrical resistivity in Fe 80 (Nb 1–x Mo x) 5 B 15 (x = 0–0.75) amorphous ribbons. *Vacuum* **2019**, *163*, 368–372. [CrossRef]
49. Li, X.; Shi, Z.; Zhang, T. Effect of similar element substitution on Fe-B-Si-Mo bulk metallic glasses studied by experiment and ab initio molecular dynamics simulation. *J. Alloys Compd.* **2019**, *784*, 1139–1144. [CrossRef]